



Contents lists available at ScienceDirect

Arabian Journal of Chemistry

journal homepage: www.ksu.edu.saPreparation of copper porphyrin photosensitized iron-based MOFs composite photocatalyst and study on CO₂ reduction performanceHaijian Yang^{a,*}, Dongmei Yang^c, Na Xiao^a, Huihui Yu^a, Haihua Yang^b, Yan Ma^c, Kelian Wu^{b,*}^a Faculty of Engineering, Huanghe Science and Technology University, Henan, Zhengzhou 450063, China^b School of Biology and Chemical Engineering/Henan Key Laboratory of Microbial Fermentation, Nanyang Institute of Technology, Henan, Nanyang 473000, China^c Department of Petroleum and Chemical, Bayingoleng Vocational and Technical College, Bazhou 841000, China

ARTICLE INFO

Keywords:

Copper porphyrin
MOFs
Photocatalyst
Cu-TCPP@MIL-101(Fe)
CO₂ reduction

ABSTRACT

Fe-based MIL-101(Fe) MOFs have a high potential to capture CO₂ due to their high porosity, porous structure, and significant interaction with CO₂, but the photogenerated electron and hole recombination phenomenon is relatively obvious. Copper tetracarboxyphenyl porphyrin (Cu-TCPP) was incorporated into MIL-101(Fe) as a photosensitive material to form a heterostructure. This enhanced the light absorption capability and the photogenerated electron-hole pairs separation in the composite catalyst. Based on the above factors, the current study reported the synthesis of MIL-101(Fe) by hydrothermal method, and a new composite photocatalyst Cu-TCPP@MIL-101(Fe) was prepared by using Cu-TCPP as a copper source with different mass ratios. The morphological and structural characterization of the composite catalyst was carried out by XRD, SEM, TEM, BET, and FT-IR, and the CO₂ reduction performance of the composite catalyst Cu-TCPP@MIL-101(Fe) was determined by a vacuum CO₂ reduction system under simulated sunlight irradiation. The results revealed that MIL-101(Fe) was loaded with Cu-TCPP with the formation of type II heterojunctions that are capable of inhibiting the electron-hole recombination with improved light absorption capacity, and accelerated reduction rate of CO₂. The reduction rate of CO₂ into CO was found to be 29 μmol·g⁻¹·h⁻¹.

1. Introduction

Energy depletion and environmental damage are caused by the ongoing consumption of fossil fuels and the immense emission of CO₂ gas as a consequence of constant and rapid societal development (Broecker et al., 1979; Schneider, 1989). The greenhouse effect is currently a major problem for the entire world. Technology-based carbon resource recycling and the utilization of renewable energy sources have been recognized as effective strategies for reducing the greenhouse effect (Panwar et al., 2011; Wang et al., 2023). Physical and chemical adsorption-based separation, photocatalytic conversion, and membrane separation are currently the most important technologies supporting carbon dioxide recycling (Das et al., 2020; Lei et al., 2018; Lin et al., 2023; Luo et al., 2023). Photocatalysis technology is a highly effective and economical technical approach utilized for the catalytic reduction of CO₂. Nevertheless, the production of appropriate photocatalytic materials poses a significant challenge (Chen et al., 2022; Huang et al., 2023; Chen et al., 2022). Materials for photocatalytic carbon dioxide reduction

are now comprised of metal-organic frameworks (MOFs) and metal complexes of the precious metals Rhodium and Ruthenium, in addition to semiconductor materials such as sulfides and oxides (Furukawa et al., 2013; Qian et al., 2021; Ren et al., 2022; Zhao et al., 2023; Ding et al., 2023).

Among MOFs materials, MIL-101 exhibits a rigid structure and high porosity. In addition, the MIL-101 series has exceptional chemical stability compared with other MOFs materials. The addition of diverse metal ions into the MIL-101 framework yields materials exhibiting distinct properties, thereby offering a wide range of opportunities for research (Chi et al., 2016; Chen et al., 2023). As a derivative of MIL-101, MIL-101(Fe) generally retains all of the original advantages of the parent material, such as the ability to regulate its structure, large specific surface area along exceptional chemical stability (Zorainy et al., 2021). Zhao et al. (Zhao et al., 2020); in 2020, synthesized MIL-101(Fe)/g-C₃N₄ heterojunction by *in-situ* growth of MIL-101(Fe) on the g-C₃N₄ surface. Heterojunctions, which are employed as bifunctional photocatalysts to increase light absorption as well as charge carrier separation, exhibited a

* Corresponding authors.

E-mail addresses: yanghj@hnhstu.edu.cn (H. Yang), Wukeliang@nyist.edu.cn (K. Wu).<https://doi.org/10.1016/j.arabjc.2024.105722>

Received 6 December 2023; Accepted 7 March 2024

Available online 8 March 2024

1878-5352/© 2024 The Author(s). Published by Elsevier B.V. on behalf of King Saud University. This is an open access article under the CC BY-NC-ND license (<http://creativecommons.org/licenses/by-nc-nd/4.0/>).

markedly improved photocatalytic performance in comparison to MIL-101(Fe) or g-C₃N₄. Aiming to enhance the efficacy of photogenerated carrier separation, researchers have directed their efforts towards developing efficient strategies to reduce photoelectron-hole recombination, which has historically been the primary factor affecting the performance of MOF materials (Chen et al., 2023; Zhao et al., 2023; Yang et al., 2022).

Copper porphyrin can effectively absorb visible light over a range of 400–700 nm, and possess remarkable visible light response. Furthermore, the presence of a metal active site within its structure significantly enhances electron transfer capability, resulting in advantageous photocatalytic performance. When the light intensity reaches a specific threshold, electron transfer is facilitated and the transferred electron contributes to the photocatalytic reduction of CO₂, thereby increasing the overall efficacy of the reduction process. (Wang et al., 2019; Fateeva et al., 2012; Zhang et al., 2021). The fabrication of novel porphyrin-based framework materials may result in a significant enhancement in their catalytic activity by an increase in the exposure of the catalytic active site. First, effective enhancement of the process involving mass transfer in porphyrin-based skeleton materials can be achieved through adjustment of the number of pores exposed to active sites. Furthermore, the growth of porphyrin-based skeleton materials on a conductive substrate resulted in the formation of conductive skeleton materials. To enhance the efficiency of the electron transfer process, electron donor and collecting nodes were incorporated. Porphyrin-based framework materials can exhibit synergistic features when combined with another guest, particularly in confined pore environments thereby enhancing their catalytic efficacy (Wang et al., 2022; Xu et al., 2020; Guo et al., 2019; Ladomenou et al., 2015). Consequently, investigating the metalloporphyrin framework in the context of photocatalytic carbon dioxide reduction holds considerable promise.

The solvent-thermal approach was utilized to synthesize Cu-TCPP@MIL-101(Fe) composite catalysts with various concentrations (2, 4, 6, 8, 10 %) to enhance the photoelectron-hole pair separation of MOFs material MIL-101(Fe) and increase the catalytic reduction efficacy of CO₂. The rational morphological structure of Cu-TCPP@MIL-101(Fe) was determined employing SEM and TEM, while the efficacy of the complex in CO₂ reduction was also assessed. The photocatalytic reaction mechanism of Cu-TCPP@MIL-101(Fe) was identified as a type II heterojunction, which significantly enhanced the separation of photogenerated electrons and holes and demonstrated improved reduction performance of CO₂.

2. Experimental section

2.1. Reagents and instruments

The drugs used in the experiment were all analytically pure. CH₂COOH propionate, C₈H₇NO₄ 2-amino-terephthalic acid, ferric chloride FeCl₃·6H₂O, Pyrrole C₄H₅N, cuprous chloride CuCl₂, 4-formylbenzoic acid C₈H₆O₃ were procured from Shanghai Maclin Biochemical Technology Co., LTD. Anhydrous ethanol CH₃CH₂OH was purchased by Sinopharm Group Chemical Reagent Co., LTD. Methanol CH₃OH was provided by Tianjin Fuchen Chemical Reagent Factory. DMF was procured from Tianjin Fuyu Company. Deionized water was used in all experiments.

The materials were investigated for their crystal structure by using a MiniFlex600 X-ray diffractometer (XRD). The characterization regarding the functional group of the materials was carried out by using Fourier transform infrared spectroscopy (Thermo Fisher Technologies). A detailed analysis of the material's morphology was carried out by transmission electron microscopy (SEM, JSM-7900F Nippon Electronics Co., LTD) and transmission electron microscopy (TEM; JEOL JEM-2100PLUS). The materials were investigated for porosity and particle size by using SSA-4300 specific surface area and aperture analyzer (BET; Beijing Biode Electronic Technology Co., LTD). Using a UV-2450 UV

diffuse reflection spectrometer (Shimadzu Co., LTD), the molecular structure of the substances was examined. The photoelectric properties of the materials were analyzed by a 760-e electrochemical workstation (Shanghai Chenhua Instrument Co., LTD). The efficacy of the carbon dioxide reduction was evaluated utilizing a xenon lamp as the light source in a vacuum carbon dioxide reduction system (MC-SCO2II-AG Beijing MGS Technology Co., LTD.).

2.2. Material preparation

2.2.1. Preparation of TCPP

The porphyrins were synthesized by using the method reported previously (Rhauderwiek et al., 2016). 4-formylbenzoic acid (6.08 g; 40.5 mmol) and pyrrole (2.8 mL, 40.5 mmol) were weighed with an electronic balance. Propionic acid solution (150 mL) was heated in an oil bath and stirred magnetically. The black reaction solution was subjected to cooling for 2 h at room temperature and then added with 200 mL methanol. The stirring was continued in an ice bath for 0.5 h. The resulting sediment was centrifuged and rinsed with methanol and distilled water until the filtrate became transparent. Finally, the resulting purple powder was kept for 12 h in an oven at 80 °C to achieve optimum drying (yield: 16 %).

2.2.2. Preparation of Cu-TCPP

The synthesis of copper(II) complex of meso-tetra(4-carboxyphenyl) porphyrin was performed by using a previously reported protocol (Lin et al., 2018). The mixture of CuCl₂ (0.245 g; 1.82 mmol) and TCPP (0.261 g, 0.33 mmol) was allowed to dissolve in 15 mL DMF (N,N-dimethylformamide), heated in an oil bath, and stirred magnetically. Following 5 h of refluxing, the red solution was allowed to cool to room temperature, resulting in the formation of a solid precipitate. After subjecting the solution containing the precipitate to centrifugation and more than five washes with water, it was dried out at 60 °C under vacuum conditions. As a consequence, a red solid was produced.

2.2.3. Preparation of Cu-TCPP@MIL-101(Fe)

FeCl₃ (135.15 mg, 0.5 mmol), NH₂-H₂BDC (90.57 mg, 0.5 mmol), and porphyrin Cu-TCPP (42.8 mg, 0.05 mmol) were weighed and dissolved in DMF (7.5 mL) and heated in an oven for 20 h at 110 °C. After being cooled at room temperature, the samples were centrifuged to collect red solids. The solids are washed thrice with DMF to remove the unreacted precursors and then exchanged with acetone three times. The resulting red powder was centrifuged and dried at 80 °C in an oven.

2.3. Carbon dioxide reduction performance test

MC-SCO2II-AG vacuum carbon dioxide reduction system produced by Beijing Maison Co., Ltd. was employed for the reduction of CO₂ feedstock gas and product gases, as well as for the quantitative analysis of gas phase products via gas chromatography with an online gas analyzer. The operation steps are as follows: 8 h in the dark after the reaction unit is pre-balanced, the reaction is performed under a 300 W xenon arc lamp (MC-PF300B), along with the use of a filter (AM 1.5G) simulating the sunlight intensity. The cooling circulating water system was used to stabilize the reaction temperature at 5 °C. The product components were detected by an FID detector, while the photocatalytic reduction products were subjected to per hour analysis for a duration of 6 h using a gas chromatograph GC9700 device.

3. Results and discussion

3.1. Structural characterization of catalysts

3.1.1. Scanning and transmission electron microscopy of composite photocatalyst

The morphology of Cu-TCPP@MIL-101(Fe) nanoparticles with

varying concentration ratios was observed using SEM and TEM, as shown in Fig. 1. Fig. 1 (a) to (f) represent the SEM micrographs of pure MIL-101(Fe), x ($x = 2\%$, 4% , 6% , 8% , 10%) Cu-TCPP@MIL-101(Fe), respectively. As evident from the figure, the load on the MIL-101(Fe) surface increases with the increase of the Cu-TCPP ratio. Moreover, MIL-101(Fe) retained good structural stability under different concentrations of Cu-TCPP (2%, 4%, 6%, 8%, 10%), which may be due to the stabilizing influence of amino ($-\text{NH}_2$) group present in MIL-101(Fe). To confirm this hypothesis, MIL-101(Fe) without an amino group was selected for the fabrication of the composite, and the structure was found to be damaged to a certain extent, and cracks appeared in MIL-101(Fe) material under the same conditions (Fig. 1g). Hence, it may be concluded that the amino ($-\text{NH}_2$) group exerts an important role in the structural stability of MOFs material MIL-101(Fe). Fig. 1(h) and (i) show the transmission electron micrographs of a 4% Cu-TCPP@MIL-101(Fe) composite catalyst. Fig. 1(h) shows a low-resolution TEM micrograph, indicating the successful loading of Cu-TCPP onto MIL-101(Fe). Both Cu-TCPP and MIL-101(Fe) were observed as amorphous materials.

3.1.2. XRD and FT-IR analysis of composite photocatalyst

Fig. 2a shows XRD patterns of Cu-TCPP, MIL-101(Fe), as well as Cu-TCPP@MIL-101(Fe) at different concentrations. It is obvious that MIL-101(Fe) possesses 6 diffraction peaks at $2\theta = 8.13^\circ$, 8.97° , 9.8° , 9.97° , 16.63° and 18.78° , which was consistent with the diffraction peaks reported in the literature at $2\theta = 8.97^\circ$, 9.8° and 16° (Sun et al., 2016). MIL-101(Fe) was successfully synthesized. The figure illustrates that Cu-TCPP@MIL-101(Fe) material retains six discernible diffraction peaks

at different concentrations, indicating that the MIL-101(Fe) material retains its strong structural integrity even after Cu-TCPP loading. The FTIR spectra of MIL-101(Fe), Cu-TCPP, and Cu-TCPP@MIL-101(Fe) are depicted in Fig. 2b. The Amide bond produces a distinctive peak in the infrared absorption spectra, giving rise to a band at $1650\text{--}1750\text{ cm}^{-1}$. This peak is referred to as the amide I peak. An additional discernible band in the range of $1250\text{--}1350\text{ cm}^{-1}$ could potentially be ascribed to the amide bond. It is frequently referred to as the amide II peak and originates from the acyl group containing oxygen, vibrating within the amide bond. The absorption peaks near 1682 , 1535.1 , and 1286 cm^{-1} , as shown in the figure, provided sufficient evidence for the reaction between amino and carboxyl groups to produce amide bonds (Zhong et al., 2023). It confirms the successful loading of NH_2 -MIL-101(Fe) onto Cu-TCPP.

3.1.3. XPS analysis of composite photocatalysts

The electronic states along with the elemental composition of Cu-TCPP@MIL-101(Fe) were detected by X-ray photoelectron spectroscopy (XPS). The actual primary elemental distribution is shown in Fig. 3 (a). High-resolution C1s spectrum (Fig. 3b) demonstrated three characteristic peaks at 284.8 , 285.3 , and 288.8 eV , which were attributed to the presence of the C-C, C-O, and C = O bonds. The spectrum of O1s primarily comprises peaks with combined energies of 532.2 , 530.5 , and 533.7 eV which may be respectively ascribed to the presence of O = C-O bonds in carboxylic groups, Fe-O bonds in clusters, and adsorbed molecules of water (Fig. 3c). There were three peak positions of 398.6 , 399.9 , and 401.1 eV in the N 1s spectrum (Fig. 3d), which were

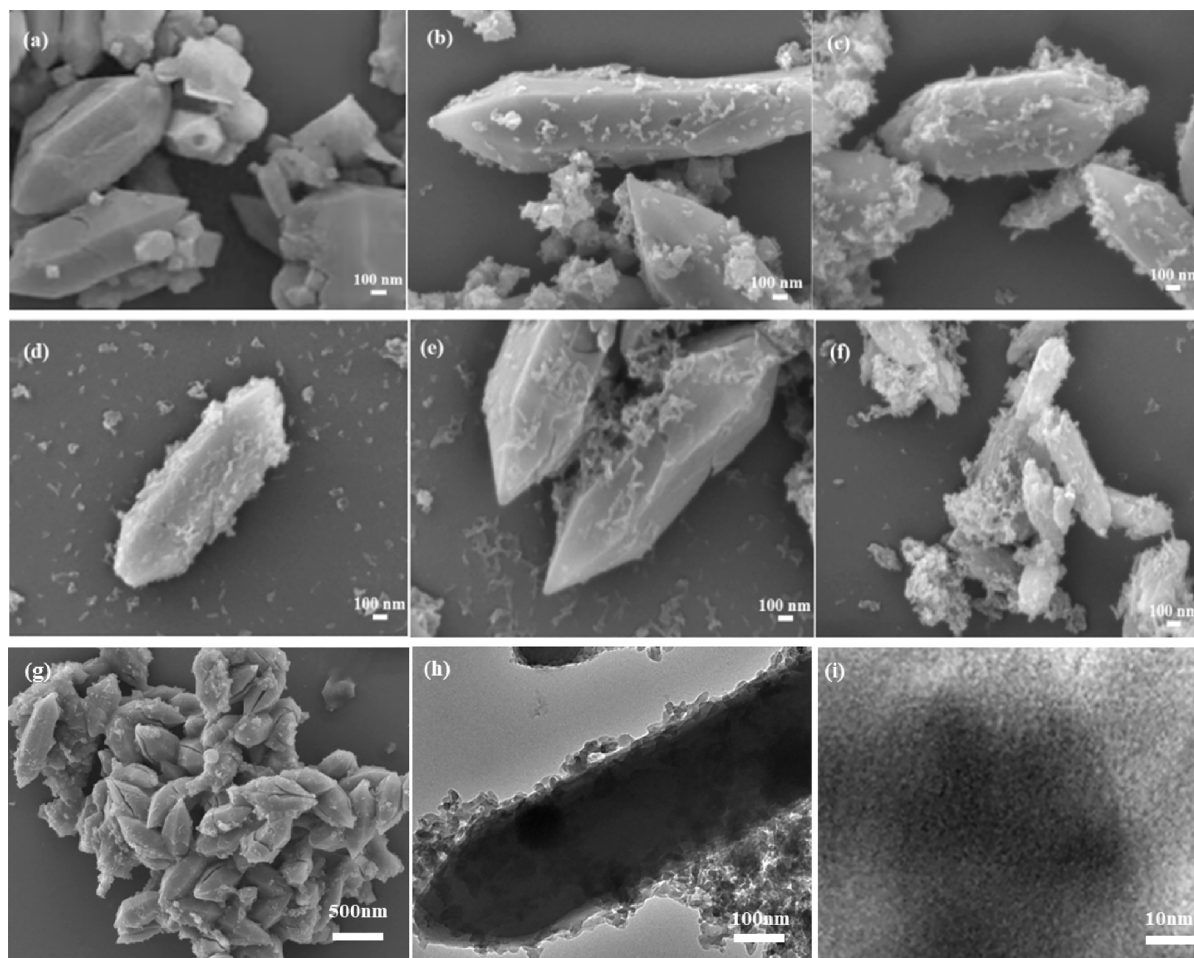


Fig. 1. Scanning and transmission electron microscopy (a) MIL-101(Fe), (b) 2% Cu-TCPP@MIL-101(Fe), (c) 4% Cu-TCPP@MIL-101(Fe), (d) 6% Cu-TCPP@MIL-101(Fe), (e) 8% Cu-TCPP@MIL-101(Fe), (f) 10% Cu-TCPP@MIL-101(Fe), (g) MIL-101 without amino group (Fe), (h) low power transmission, (i) high power transmission.

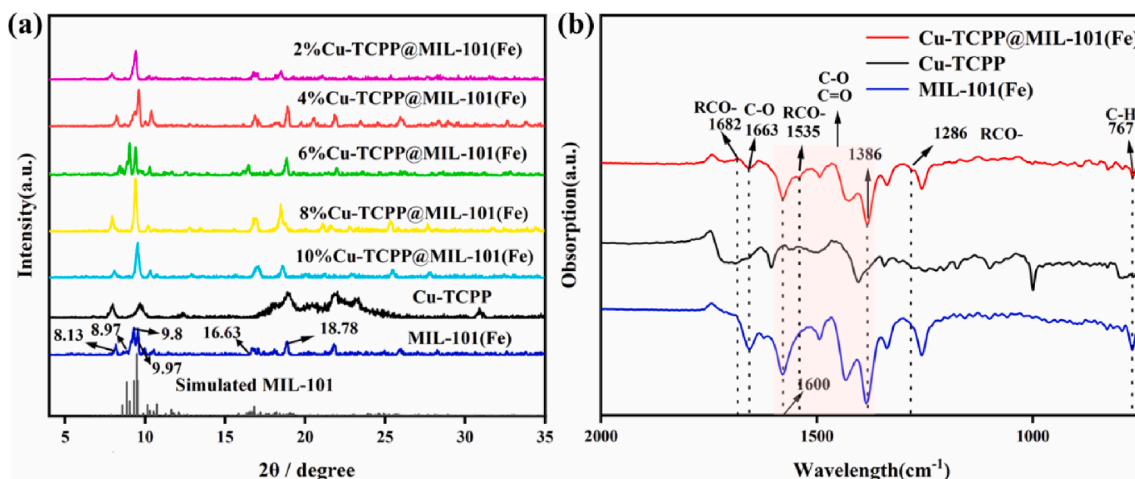


Fig. 2. (a) XRD pattern of the composite and (b) FT-IR spectrum of the composite.

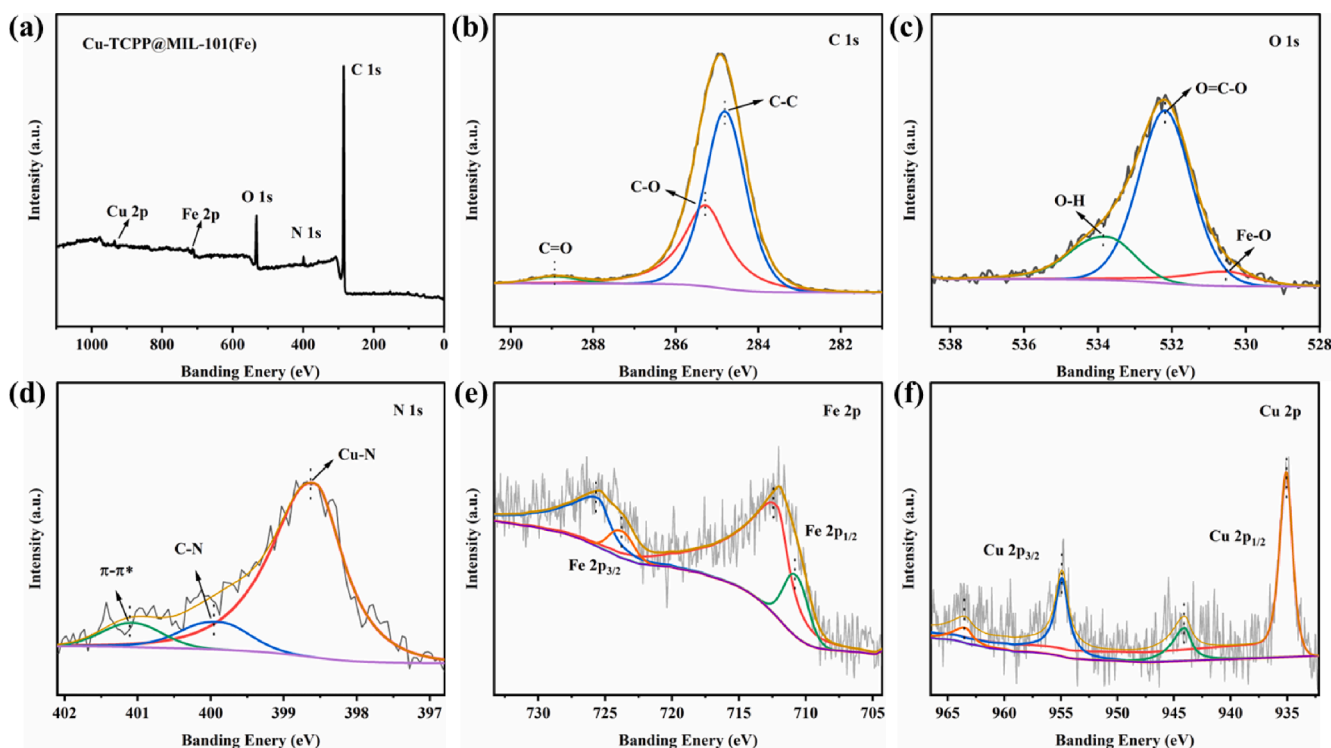


Fig. 3. XPS spectrogram of Cu-TCPP@MIL-101(Fe), (a) survey spectra, (b) C 1 s, (c) O 1 s, (d) N 1 s, (e) Fe 2p, (f) Cu 2p.

attributed to the satellite peaks of the Cu-N, C-N, and π - π^* bond in the benzene ring, respectively. The Fe 2p_{3/2} and Fe 2p_{1/2} peaks were evident in the Fe 2p spectrum near 711 eV and 724 eV, respectively (Fig. 3e). Particularly, the fitting peaks at 710.7, 712.1, 723.8, and 725.5 eV reflect the usual spectral peaks of Fe³⁺, indicating the presence of a large amount of trivalent iron in the composite. Fig. 3(f) shows the Cu 2p spectrum, where the peak of Cu 2p_{1/2} appeared at 935.1 eV, Cu 2p_{3/2} at 954.9 eV, and the satellite peaks at 944.1 eV and 963.4 eV were attributed to the presence of Cu²⁺.

3.1.4. BET analysis of composite photocatalyst

Fig. 4(a) shows the isothermal adsorption-desorption curves of nitrogen. It is apparent from the figure that the adsorption and desorption curves of 2, 4, 6, 8, and 10 %Cu-TCPP@MIL-101(Fe) in the high-pressure region demonstrated obvious hysteresis curves. These curves correspond to the type IV adsorption curve, which signifies that the

corresponding materials were mesoporous in nature. Fig. 4(b) shows the average aperture distribution curve. Most of the apertures of Cu-TCPP@MIL-101(Fe) were distributed between 10 and 20 nm. Table 1 provides detailed information on the average pore diameter, pore volume, and specific surface area of Cu-TCPP@MIL-101(Fe) based on the loaded quantity. Notably, the average pore diameter as well as the specific surface area of the composite material decreases with an increase in Cu-TCPP load. Presumably, this finding may be ascribed to the obstruction of the pore structure made possible by the addition of Cu-TCPP.

3.2. Characterization of photocatalytic properties

3.2.1. Uv-vis absorption spectra of composite catalysts

Fig. 5(a) demonstrates the UV-VIS absorption spectra of MIL-101(Fe), Cu-TCPP, 4 % Cu-TCPP@MIL-101(Fe). The figure revealed that

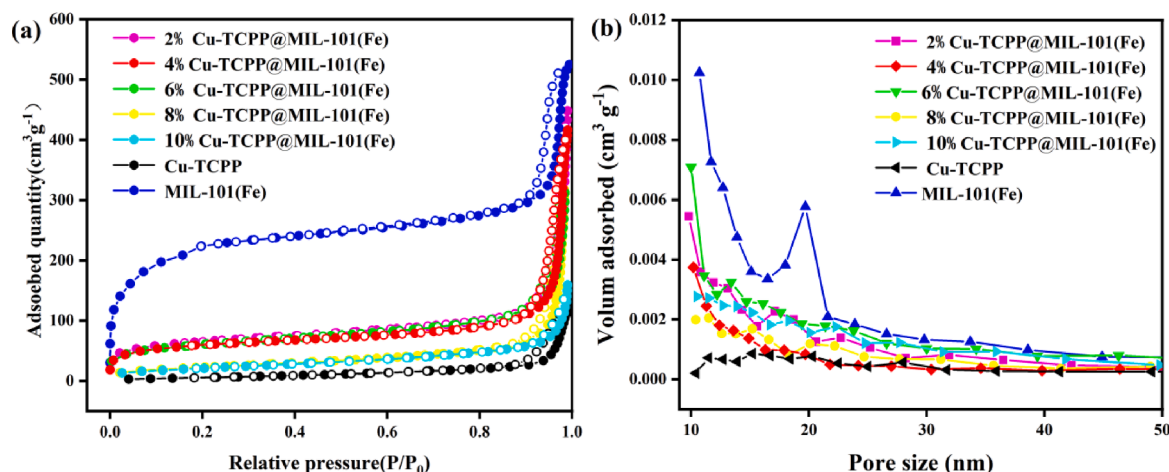


Fig. 4. (a) N_2 adsorption/analytic isotherm of the sample and (b) pore size distribution method for the sample.

Table 1

Specific surface area, pore volume, and aperture of different catalysts.

Sample name	Specific surface area (m^2/g)	Pore volume (cm^3/g)	Average pore size (nm)
2 % Cu-TCPP@MIL-101(Fe)	228.143	0.697109	11.74
4 % Cu-TCPP@MIL-101(Fe)	213.172	0.647295	6.26
6 % Cu-TCPP@MIL-101(Fe)	211.729	0.485533	6.11
8 % Cu-TCPP@MIL-101(Fe)	84.157	0.493972	6.07
10 % Cu-TCPP@MIL-101(Fe)	79.090	0.247478	4.59
Cu-TCPP	25.626	0.190973	2.11
MIL-101(Fe)	774.857	0.816461	14.90

the absorption band edge of MIL-101(Fe), Cu-TCPP, and 4% Cu-TCPP@MIL-101(Fe) was 546, 760, and 732 nm respectively. Cu-TCPP exhibited two peaks at 376.88 and 540 nm, while 4 % Cu-TCPP@MIL-101(Fe) also revealed two absorption peaks at 418 and 540 nm, indicating the successful loading of porphyrin Cu-TCPP onto the surface of MIL-101(Fe) material. However, 4 % Cu-TCPP@MIL-101(Fe) exhibited a certain deviation from Cu-TCPP and MIL-101(Fe), which may be ascribed to the role of amino groups and carboxyl groups. The absorption of the sample at different wavelengths can be obtained through

UV-Vis analysis, which can be calculated according to formula 1 and plotted against $h\nu$ with $(\alpha h\nu)^{1/n}$. As shown in Fig. 4b, the linear part of the obtained graph is extruded to the horizontal axis, and the intersection point represents the band-gap width value (Zhong et al., 2023).

$$(\alpha h\nu)^{1/n} = A(h\nu - E_g) \quad (1)$$

α is the absorption index, h , and ν respectively represent Planck's constant and frequency, E_g is the semiconductor bandgap width, and A is a constant. The semiconductor bandgap is illustrated in Fig. 5(b), where the bandgap value of 4 % Cu-TCPP@MIL-101(Fe) was identified as 1.73 eV, indicating the remarkable capacity of material for light absorption, which may be ascribed to the addition of Cu-TCPP. The light absorption capacity of the composite material was enhanced due to the long-wave orientation of the edge of its light absorption band. It is beneficial to improve the utilization rate of solar energy.

3.2.2. Photoelectric properties of composite photocatalysts

Fig. 6a shows the transient photocurrent response spectrum of Cu-TCPP@MIL-101(Fe) photocatalyst at different concentrations, under a 300 W Xe lamp. Cu-TCPP@MIL-101(Fe) material generates photoelectrons and photogenerated holes under the influence of light. Inadequate separation efficiency results in the recombination of photoelectrons and photogenerated holes, leading to a weak photocurrent. Greater charge separation efficiency and electron-hole separation capability are associated with increased photocurrent intensity. Fig. 6b

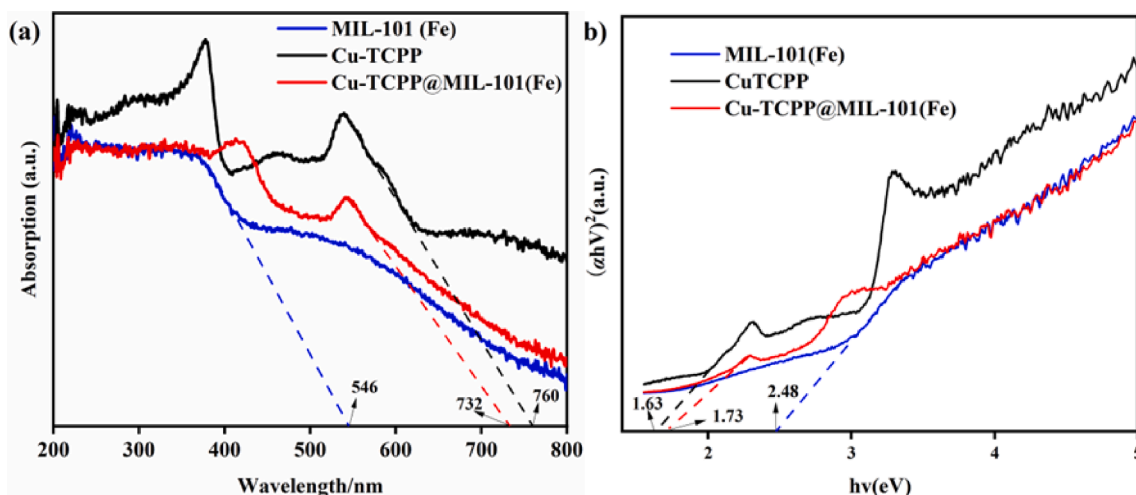


Fig. 5. (a) Spectra of diffuse UV-vis reflectance for various samples, (b) Band gap diagram.

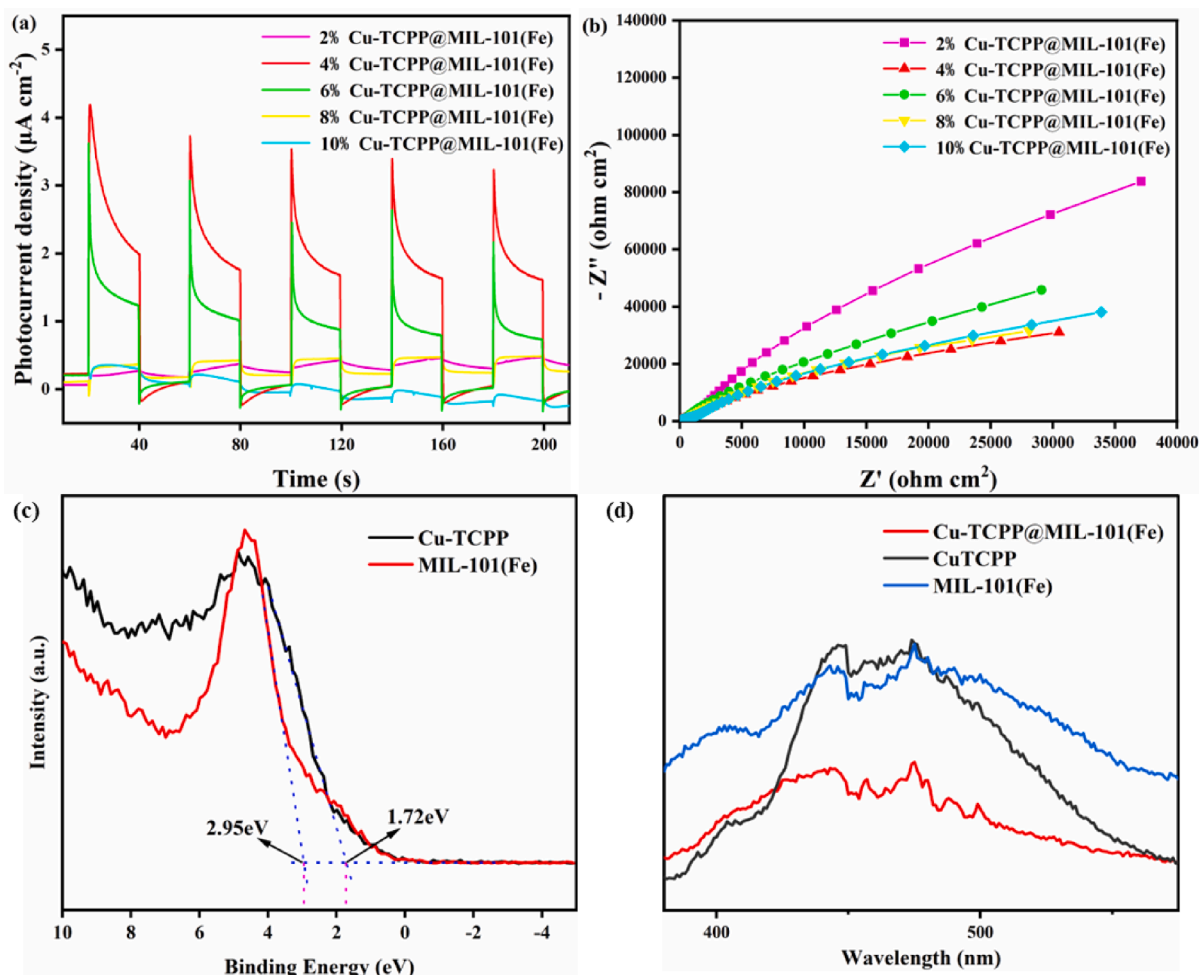


Fig. 6. (a) Photoelectric performance of the composite catalyst at each stage (a) i-t diagram (b) EIS diagram (c) XPS valence band spectra (d) PL spectrum.

shows the AC impedance curve of 4 % Cu-TCPP@MIL-101(Fe). A larger amplification curve signifies a reduced radius, which consequently corresponds to a small impedance value, providing further evidence of the best separation effect. Fig. 6c shows the xps valence band spectrum, from which it can be seen that the valence band position of CuTCPP was $E_{VB,XPS} = 1.72$ eV, while the valence band position of MIL-101(Fe) was determined as $E_{VB,XPS} = 2.95$ eV. Currently, only the valence band position in relation to the vacuum level is being measured. Therefore, formula 2 must be used to determine the valence band position of the material in relation to the hydrogen electrode (standard). The calculated valence band position of CuTCPP was $E_{VB,NHE} = 0.67$ eV, and MIL-101(Fe) was $E_{VB,NHE} = 1.9$ eV. The band gap values of MIL-101(Fe) and Cu-TCPP were respectively determined as 2.48 and 1.63 eV when combined with UV-vis spectra. Therefore, the conduction band of MIL-101(Fe) and Cu-TCPP was found to be -0.58 and -0.96 eV respectively. To accomplish the effective electron-hole separation effect, the charge transfer mechanism conforms to the type II heterojunction and transfers conduction band electrons from lower to higher positions and valence band holes from higher to lower positions. (Kahn, 2016) Fig. 6d shows the photoluminescence spectrum. Recombination of electrons and holes occurs at a slower rate when the PL intensity decreases under specific conditions. It can be seen from the results that the photoluminescence intensity of Cu-TCPP@MIL-101(Fe) was significantly reduced as compared to MIL-101(Fe) and CuTCPP. Carrier recombination is generally regarded as more probable when the intensity of the PL increases. The observed decrease in PL strength signifies a substantial inhibition of medium electron-hole recombination and an increase in charge separation efficiency in the composite (Li et al., 2021).

$$E_{VB,NHE} = \varphi + E_{VB,XPS} - 4.85eV \quad (2)$$

φ represents the work function associated with the XPS analyzer.

3.2.3. Photocatalytic activity of composite catalyst

An assessment was conducted on the photocatalytic performance of composite catalysts containing different amounts of Cu-TCPP to ascertain the relationship between Cu-TCPP load and photocatalytic activity. The photocatalytic activity of the MIL-101(Fe) in reducing CO_2 was initially weak, as shown in Fig. 7 but improved after being added with Cu-TCPP. The best CO_2 reduction impact was observed in samples with a 4 % Cu-TCPP@MIL-101(Fe) ratio, and the yield of CO was observed as $68 \mu\text{mol/g}$. It is 1.92 times greater than the value of $35.4 \mu\text{mol/g}$ for MIL-101(Fe) and much higher in comparison to that of other ratios of Cu-TCPP@MIL-101(Fe). The stability of the composite photocatalyst was determined using 4 % Cu-TCPP@MIL-101(Fe) composite for multiple cycles of photocatalytic CO_2 reduction, with good performance following 5 cycles, as shown in Fig. 7c. The moderate stability of the composite photocatalyst was indicated by the fact that its capacity to reduce CO_2 decreased slightly with increasing number of cycle. A bandpass filter was utilized to quantify the apparent quantum yield (AQY) of CO_2 evolution. The calculation is performed utilizing Formula 3, which is dependent on the quantity of oxygen gases generated by the photocatalytic reaction within an hour (Lin et al., 2020):

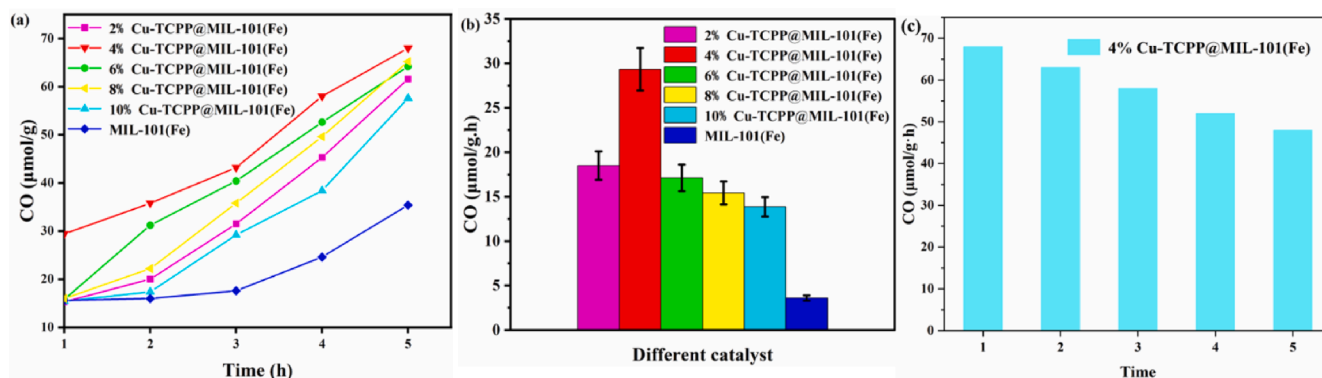


Fig. 7. (a) Cu-TCPP@MIL-101(Fe) CO₂ reduction performance at different time periods (b) Bar chart of CO₂ reduction rate (c) Durability measurements (5 h test per cycle).

$$AQY = \frac{Ne}{N_p} \times 100\% = \frac{10^9(v \times N_A \times K) \times (h \times c)}{(I \times S \times \lambda)} \times 100\%$$

$$= \frac{1.2 \times 10^8(v \times K)}{(I \times S \times \lambda)} \times 100\% \quad (3)$$

In this work, the apparent quantum yield (AQY) was measured by applying an Xe lamp (300 W) with an AM1.5G band-pass filter. The calculated AQY value was determined to be 0.13 %.

N_e : total number of electrons transferred, N_p : number of incident photons, v : reaction rate (1.9×10^{-8} mol/s), K : number of electrons transferred, N_A is Avogadro constant (6.02×10^{23} /mol), c and h respectively represent the speed of light (3×10^8 m/s) and Planck constant (6.62×10^{-34} J·s), S is the irradiation area (m^2), I is the intensity of irradiation light (W/m^2), λ is the wavelength of the incident light.

3.2.4. Photocatalytic mechanism

Fig. 8 shows the mechanism of CO₂ reduction by complex Cu-TCPP@MIL-101(Fe). Photoexcitation occurs when MIL-101(Fe) is exposed to light where the energy of the light source surpasses the corresponding band gap (E_g). This induces the migration of photo-generated electrons from the valence band VB to the conduction band CB, leaving photo-generated holes behind. Conduction band electrons migrated from lower to higher positions, while the valence band holes migrated from higher to lower positions. The valence band spectrum and UV-vis spectrum indicate that the conduction position of MIL-101(Fe) was -0.58 eV at 1.90 eV and that of Cu-TCPP was -0.96 eV at 0.67 eV. Due to the lower valence band of Cu-TCPP in comparison to MIL-101(Fe), holes could potentially migrate to the Cu-TCPP valence band,

resulting in the consumption of the hole sacrificial agent. Cu-TCPP possessed a higher conduction band than MIL-101(Fe), suggesting that photogenerated electrons from Cu-TCPP might migrate to the guide band of MIL-101(Fe), thereby converting CO₂ to CO. The Cu-TCPP@MIL-101(Fe) composites conform to the charge transfer mechanism of type II heterojunctions and achieve effective electron-hole separation, thereby improving the catalytic performance of composite catalysts.

3.2.5. Comparison of performance of photocatalytic CO₂ reduction catalysts

Table 2 lists the relevant studies of MOF materials utilized in the photocatalytic reduction of CO₂, which include catalytic materials, light sources, reaction conditions, and CO production. The composite catalyst Cu-TCPP@MIL-101(Fe) was developed in this study to reduce CO₂ under visible light, under relatively simple reaction conditions, and with a CO yield of the reduction product exceeding the medium level, in contrast to previous research.

4. Conclusion

In conclusion, a type II heterojunction was formed by permitting MIL-101(Fe) and Cu-TCPP to interact via amide bonds to enhance the utilization rate of sunlight and assist the separation of photogenerated electrons and holes in MIL-101(Fe). The resultant heterojunction enhanced the efficiency of the photocatalytic process by inhibiting electron-hole recombination while extending the light absorption band edge. The potential mechanism for photocatalytic CO₂ reduction was

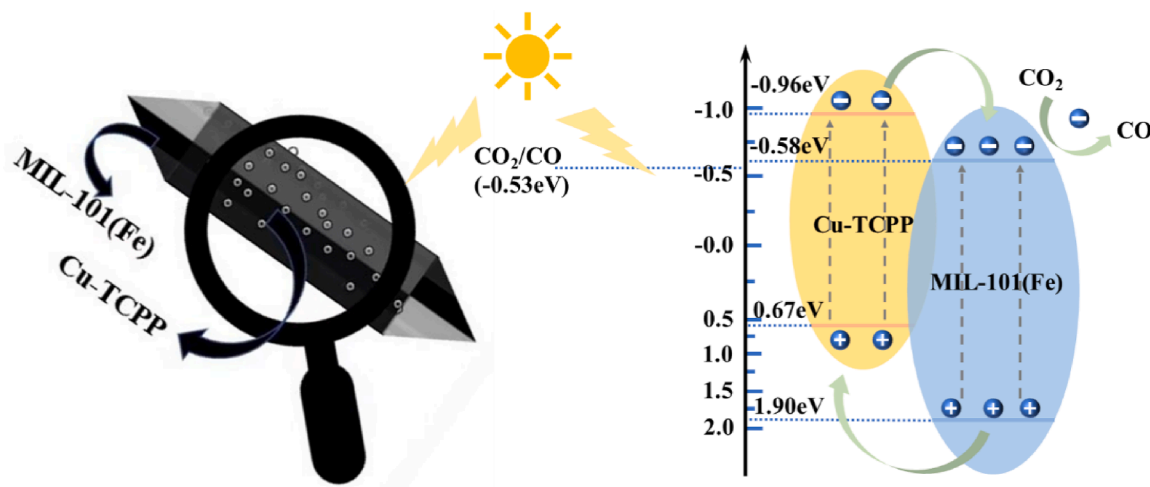


Fig. 8. Photocatalytic reduction mechanism of CO₂.

Table 2
Comparison of performance of photocatalytic CO₂ reduction catalysts.

Photocatalyst	Light source	Experimental conditions	Products (yields in μmol/g/h)	Ref.
Cu-TCPP@MIL-101 (Fe)	300 W Xenon lamp (λ = 400–760 nm)	2 mL H ₂ O P = 80 kPa, t = 6 h	CO (29)	This work
MAF-X27-OH	λ = 420 nm	4:1 CH ₃ CN/H ₂ O, [Ru(bpy) ₃]Cl ₂ , TEOA, t = 10 h, P = 1 atm	CO (21), H ₂ (0.6)	(Wang et al., 2018)
MIL-101-EN	Xenon lamp (330 nm)	P = 71 kPa, V = 500 mL, t = 10 h	CO (47.2), CH ₄ (1.8)	(Xie et al., 2019)
NH ₂ -UiO-66	λ > 420 nm	Solution containing 1.0 μmol [Ru(bpy) ₃]Cl ₂ ·6H ₂ O, 5 mL H ₂ O and acetonitrile, 1:4 v/v ratio, 1 mL	CO (1.2), H ₂ (2.2)	(Wang et al., 2014)
Ni MOFs	λ = 420 nm	[Ru(bpy) ₃]Cl ₂ ·6H ₂ O, TEOA, t = 2 h	CO (12.5), H ₂ (0.28)	(Han et al., 2018)
UiO-66/CNNs	300 W Xenon lamp (λ = 400–800 nm)	5 mL TEOA and MeCN in 1:4 v/v ratio, P = 80 kPa, V = 330 mL	CO (9.9)	(Shi et al., 2015)

proposed through the utilization of valence band spectra from UV–vis and XPS to calculate the band positions of the composites. A novel Cu-TCPP composite photocatalyst Cu-TCPP@MIL-101(Fe) was synthesized using various mass ratios under solvothermal conditions followed by morphological and structural characterization of the composite catalyst. The findings revealed that MIL-101(Fe) loaded with 4 %Cu-TCPP exhibited significant charge separation efficiency and exceptional photocatalytic performance, resulting in a CO₂ to CO reduction yield of 68 μmol/g.

Author contributions

Haijian Yang contributed to the conception of the study and design of methodology; Na Xiao and Huihui Yu performed the experiment; Ma Yan and Yang Dongmei provided part of the experimental funds; Haihua Yang and Keliang Wu performed the data analyses and wrote the manuscript.

Funding declaration and acknowledgements

The authors disclosed receipt of the following financial support for the research, authorship, and/or publication of this article: This work was supported by the Anhui Yansheng New Material Co., Ltd. School-Enterprise Cooperation Project (202204610954), Tianshan Youth Grassroots Science and Technology Youth Project Mechanism Study on the Influence of Sulfur Elements in Coal in Bazhou Region on Coal-oil Co refining Hydrogenation Catalytic Reaction (2019Q137) and Open subject of Henan Key Laboratory of microbial fermentation (HIMFT20210204).

Appendix A. Supplementary data

Supplementary data to this article can be found online at <https://doi.org/10.1016/j.arabjc.2024.105722>.

References

Broecker, W.S., Takahashi, T., Simpson, H.J., Peng, T.-H., 1979. Fate of fossil fuel carbon dioxide and the global carbon budget. *Science* 206, 409–418.

- Chen, J., Abazari, R., Adegoke, K.A., Maxakato, N.W., Bello, O.S., Tahir, M., Tasleem, S., Sanati, S., Kirillov, A.M., Zhou, Y., 2022. Metal-organic frameworks and derived materials as photocatalysts for water splitting and carbon dioxide reduction. *Coord. Chem. Rev.* 469, 214664.
- Chen, Z., Kirlikovali, K.O., Li, P., Farha, O.K., 2022. Reticular chemistry for highly porous metal-organic frameworks: the chemistry and applications. *Acc. Chem. Res.* 55, 579–591.
- Chen, J., Qin, C., Mou, Y., Cao, Y., Chen, H., Yuan, X., Wang, H., 2023. Linker regulation of iron-based MOFs for highly effective Fenton-like degradation of refractory organic contaminants. *Chem. Eng. J.* 459, 141588.
- Chen, W., Zhang, W.J., Wang, K., et al., 2023. Oxygen vacancy-mediated CuWO₄/CuBi₂O₄ samples with efficient charge transfer for enhanced catalytic activity toward photodegradation of pharmacologically active compounds. *Langmuir* 39 (49), 17830–17843.
- Chi, L., Xu, Q., Liang, X., Wang, J., Su, X., 2016. Iron-based metal-organic frameworks as catalysts for visible light-driven water oxidation. *Small* 12, 1351–1358.
- Das, S., Pérez-Ramírez, J., Gong, J., Dewangan, N., Hidajat, K., Gates, B.C., Kawi, S., 2020. Core-shell structured catalysts for thermocatalytic, photocatalytic, and electrocatalytic conversion of CO₂. *Chem. Soc. Rev.* 49, 2937–3004.
- Ding, Z., Li, X., Kang, C., Yan, S., Zhao, D., Cai, H., Zhang, S.-Y., Zeng, Y.-J., 2023. Single ru atoms confined into MOF/C₃N₄ for dual improved photocatalytic carbon dioxide reduction and nitrogen fixation. *Chem. Eng. J.* 473, 145256.
- Fateeva, A., Chater, P.A., Ireland, C.P., Tahir, A.A., Khimiyak, Y.Z., Wiper, P.V., Darwent, J.R., Rossinsky, M.J., 2012. A water-stable porphyrin-based metal-organic framework active for visible-light photocatalysis. *Angew. Chem. Int. Ed.* 51, 7440–7444.
- Furukawa, H., Cordova, K.E., O’Keeffe, M., Yaghi, O.M., 2013. The chemistry and applications of metal-organic frameworks. *Science* 341, 1230444.
- Guo, X., Li, X., Qin, L., Kang, S.-Z., Li, G., 2019. A highly active nano-micro hybrid derived from cu-bridged TiO₂/porphyrin for enhanced photocatalytic hydrogen production. *Appl Catal B* 243, 1–9.
- Han, B., Ou, X., Deng, Z., Song, Y., Tian, C., Deng, H., Xu, Y.-J., Lin, Z., 2018. Nickel metal-organic framework monolayers for photoreduction of diluted CO₂: metal-node-dependent activity and selectivity. *Angew. Chem. Int. Ed.* 57 (51), 16811–16815.
- Huang, J.-M., Zhang, X.-D., Huang, J.-Y., Zheng, D.-S., Xu, M., Gu, Z.-Y., 2023. MOF-based materials for electrochemical reduction of carbon dioxide. *Coord. Chem. Rev.* 494, 215333.
- Kahn, A., 2016. Fermi level, work function and vacuum level. *Mater. Horiz.* 3 (1), 7–10.
- Ladomenou, K., Natali, M., Iengo, E., Charalampidis, G., Scandola, F., Coutsolelos, A.G., 2015. Photochemical hydrogen generation with porphyrin-based systems. *Coord. Chem. Rev.* 304–305, 38–54.
- Lei, Z., Xue, Y., Chen, W., Qiu, W., Zhang, Y., Horike, S., Tang, L., 2018. MOFs-based heterogeneous catalysts: new opportunities for energy-related CO₂ conversion. *Adv. Energy Mater.* 8, 1801587.
- Li, X., Kang, B., Dong, F., Zhang, Z., Luo, X., Han, L., Huang, J., Feng, Z., Chen, Z., Xu, J., Peng, B., Wang, Z.L., 2021. Enhanced photocatalytic degradation and H₂/H₂O₂ production performance of S-pCN/WO₂. S-scheme heterojunction with appropriate surface oxygen vacancies. *Nano Energy* 81, 105671.
- Lin, L., Hou, C., Zhang, X., Wang, Y., Chen, Y., He, T., 2018. Highly efficient visible-light driven photocatalytic reduction of CO₂ over g-C₃N₄ nanosheets/tetra(4-carboxyphenyl)porphyrin IRON(III) chloride heterogeneous catalysts. *Appl Catal B* 221, 312–319.
- Lin, H., Zhang, K., Yang, G., Li, Y., Liu, X., Chang, K., Xuan, Y., Ye, J., 2020. Ultrafine nano 1T-MoS₂ monolayers with NiOx as dual co-catalysts over TiO₂ photoharvester for efficient photocatalytic hydrogen evolution. *Appl Catal B* 279, 119387.
- Lin, H., Yang, Y., Hsu, Y.-C., Zhang, J., Welton, C., Afolabi, I., Loo, M., Zhou, H.-C., 2023. Metal-organic frameworks for water harvesting and concurrent carbon capture: areview for hygroscopic materials. *Adv. Mater.* 2209073.
- Luo, T., Gilmanova, L., Kaskel, S., 2023. Advances of MOFs and COFs for photocatalytic CO₂ reduction, H₂ evolution and organic redox transformations. *Coord. Chem. Rev.* 490, 215210.
- Panwar, N.L., Kaushik, S.C., Kothari, S., 2011. Role of renewable energy sources in environmental protection: a review. *Renew. Sustain. Energy Rev.* 15, 1513–1524.
- Qian, Y., Zhang, F., Pang, H., 2021. A review of MOFs and their composites-based photocatalysts: synthesis and applications. *Adv. Funct. Mater.* 31, 2104231.
- Ren, Y., Foo, J.J., Zeng, D., Ong, W.-J., 2022. ZnIn₂S₄ based nanostructures in artificial photosynthesis: insights into photocatalytic reduction toward sustainable energy production. *Small Structures* 3, 2200017.
- Rhaderwick, T., Waitschat, S., Wuttke, S., Reinsch, H., Bein, T., Stock, N., 2016. Nanoscale synthesis of two porphyrin-based MOFs with gallium and indium. *Inorg. Chem.* 55, 5312–5319.
- Schneider, S.H., 1989. The Greenhouse Effect: Science and Policy, *Science* 243, 771–781.
- Shi, L., Wang, T., Zhang, H., Chang, K., Ye, J., 2015. Electrostatic self-assembly of nanosized carbon nitride nanosheet onto a zirconium metal-organic framework for enhanced photocatalytic CO₂ reduction. *Adv. Funct. Mater.* 25 (33), 5360–5367.
- Sun, Y., Sun, L., Feng, D., Zhou, H.-C., 2016. An in situ one-pot synthetic approach towards multivariate zirconium MOFs. *Angew. Chem. Int. Ed.* 55, 6471–6475.
- Wang, Y., Huang, N.-Y., Shen, J.-Q., Liao, P.-Q., Chen, X.-M., Zhang, J.-P., 2018. Hydroxide ligands cooperate with catalytic centers in metal-organic frameworks for efficient photocatalytic CO₂ reduction. *J. Am. Chem. Soc.* 140 (1), 38–41.
- Wang, L., Jin, P., Duan, S., She, H., Huang, J., Wang, Q., 2019. In-situ incorporation of COPPER(II) porphyrin functionalized zirconium MOF and TiO₂ for efficient photocatalytic CO₂ reduction. *Science Bulletin* 64, 926–933.

- Wang, S., Yao, W., Lin, J., Ding, Z., Wang, X., 2014. Cobalt imidazolate metal-organic frameworks photosplit CO₂ under mild reaction conditions. *Angew. Chem. Int. Ed.* 53 (4), 1034–1038.
- Wang, S., Wang, L., Wang, D., Li, Y., 2023. Recent advances of single-atom catalysts in CO₂ conversion. *Energy Environ. Sci.* 16, 2759–2803.
- Wang, X., Zhu, L., Lv, Z., Qi, Z., Xu, Y., Miao, T., Fu, X., Li, L., 2022. Coupled visible-light driven photocatalytic reactions over porphyrin-based MOF materials. *Chem. Eng. J.* 442, 136186.
- Xie, Y., Fang, Z., Li, L., Yang, H., Liu, T.-F., 2019. Creating chemisorption sites for enhanced CO₂ photoreduction activity through alkylamine modification of MIL-101-cr. *ACS Appl. Mater. Interfaces* 11 (30), 27017–27023.
- Xu, J., Liu, X., Zhou, Z., Xu, M., 2020. Photocatalytic CO₂ reduction catalyzed by metalloporphyrin: understanding of cobalt and nickel sites in activity and adsorption. *Appl. Surf. Sci.* 513, 145801.
- Yang, H., Zhao, Z.C., Yang, Y.P., et al., 2022. Defective WO₃ nanoplates controllably decorated with MIL-101 (Fe) nanoparticles to efficiently remove tetracycline hydrochloride by S-scheme mechanism. *Sep. Purif. Technol.* 300, 121846.
- Zhang, X., Wasson, M.C., Shayan, M., Berdichevsky, E.K., Ricardo-Noordberg, J., Singh, Z., Papazyan, E.K., Castro, A.J., Marino, P., Ajoyan, Z., Chen, Z., Islamoglu, T., Howarth, A.J., Liu, Y., Majewski, M.B., Katz, M.J., Mondloch, J.E., Farha, O.K., 2021. A historical perspective on porphyrin-based metal-organic frameworks and their applications. *Coord. Chem. Rev.* 429, 213615.
- Zhao, F., Liu, Y., Hammouda, S.B., Doshi, B., Guijarro, N., Min, X., Tang, C.-J., Sillanpää, M., Sivula, K., Wang, S., 2020. MIL-101(Fe)/g-C₃N₄ for enhanced visible-light-driven photocatalysis toward simultaneous reduction of CR(VI) and oxidation of bisphenol A in aqueous media. *Appl. Catal. B* 272, 119033.
- Zhao, Z.C., Wang, K., Chang, L., et al., 2023. Construction of S-scheme MIL-101 (Fe)/Bi₂MoO₆ heterostructures for enhanced catalytic activities towards tetracycline hydrochloride photodegradation and nitrogen photofixation. *Sol. Energy* 264, 112042.
- Zhao, Z., Wang, Z., Zhang, J., Shao, C., Dai, K., Fan, K., Liang, C., 2023. Interfacial chemical bond and oxygen vacancy-enhanced In₂O₃/CdSe-Deta S-scheme heterojunction for photocatalytic CO₂ conversion. *Adv. Funct. Mater.* 33, 2214470.
- Zhong, H., Pan, F., Yue, S., Qin, C., Hadjiev, V., Tian, F., Liu, X., Lin, F., Wang, Z., Bao, J., 2023. Idealizing tauc plot for accurate bandgap determination of semiconductor with ultraviolet-visible spectroscopy: a case study for cubic boron arsenide. *J. Phys. Chem. Lett.* 14 (29), 6702–6708.
- Zorainy, M.Y., Gar Alalm, M., Kaliaguine, S., Boffito, D.C., 2021. Revisiting the MIL-101 metal-organic framework: design, synthesis, modifications, advances, and recent applications. *J. Mater. Chem. A* 9, 22159–22217.